Supplemental Document

Optics Letters

Speckle illumination SFDI for projector-free optical property mapping: supplement

MASON T. CHEN, MELINA PAPADAKIS, AND NICHOLAS J. DURR*

Department of Biomedical Engineering, Johns Hopkins University, 3400 N. Charles Street, Baltimore, Maryland 21218, USA
**Corresponding author: ndurr@jhu.edu*

Supplement DOI: https://doi.org/10.6084/m9.figshare.13519157

Parent Article DOI: https://doi.org/10.1364/OL.411187

Speckle illumination spatial frequency domain imaging for projector-free optical property mapping: supplementary material

MASON T. CHEN[1], MELINA PAPADAKIS[1], AND NICHOLAS DURR[1,*]

[1] *Department of Biomedical Engineering, Johns Hopkins University, 3400 N. Charles Street, Baltimore, MD, 21218, USA*
[*] *Corresponding author: ndurr@jhu.edu*

This document provides supplementary information to "Speckle illumination spatial frequency domain imaging for projector-free optical property mapping".

1. DETAILED SI-SFDI ALGORITHM

Here we describe the detailed algorithm of Speckle Illumination Spatial Frequency Domain Imaging (si-SFDI) to calculate optical properties from laser speckle images. For each speckle pattern I_i, we first apply a median filter with a kernel size of 3 pixels to reduce shot noise. The DC parameter is then estimated as:

$$M_{DC} = \frac{\sum_{i=1}^{N} I_i}{N}, \tag{S1}$$

which is smoothed using another median filter to generate an M_{DC} map. In our case, we chose a kernel size of 7 pixels, which was the average distance between speckle grains. The estimated M_{DC} is subtracted from each I_i to isolate tissue response to spatially varying speckle patterns. We subsequently iterate through each image with a step size of 11 pixels to extract 73×73-pixel sliding windows ($w_i(x, y)$). This window size corresponds to a frequency resolution of $0.2\ mm^{-1}$. The lowest non-zero spatial frequency resolvable by the sliding window is inversely related to the window size. To achieve a finer spatial frequency resolution, a larger window would be needed, but this would come at the expense of a lower spatial resolution of the reconstructed optical property maps. The step size of the sliding window depends on the desired resolution and computational resources. For samples with high levels of heterogeneity, a smaller step size may be preferred for higher resolution, at the cost of a longer computational time. The autocorrelation function (ACF) of each window is calculated using the Wiener-Khinchin theorem:

$$a_{w_i}(x, y) = \mathcal{F}^{-1}[W_i^*(k_x, k_y) \cdot W_i(k_x, k_y)], \tag{S2}$$

where $W_i(k_x, k_y)$ and $W_i^*(k_x, k_y)$ stand for the Fourier transform of the extracted window and its complex conjugate, respectively. For each window, we compute the mean of the ACFs across N speckle patterns:

$$a_w(x, y) = \frac{\sum_{i=1}^{N} a_{w_i}(x, y)}{N}, \tag{S3}$$

and radially average $a_w(x, y)$ to produce an ACF curve ($a_w(r)$). The power spectral density (PSD) is then computed as its Fourier transform:

$$S_W(k_r) = \mathcal{F}[a_w(r)]. \tag{S4}$$

We define the high spatial frequency response parameter as:

$$M_{AC} = \int_{0.1}^{0.5} \sqrt{S_W(k_r)} dk_r, \tag{S5}$$

which is the sum of the frequency response corresponding to the first two non-zero points of the PSD ($0.1mm^{-1} \leq k_r \leq 0.5mm^{-1}$).

After repeating the same steps for a reference phantom with known optical properties, the AC and DC diffuse reflectance (R_d) of the new sample can be calculated as:

$$R_d = \frac{M}{M_{ref}} \cdot R_{d,ref,pred}. \tag{S6}$$

In this calibration, $R_{d,ref,pred}$ denotes the diffuse reflectance of the reference phantom predicted by Monte-Carlo simulations [1]. Finally, the optical properties can be found using a pixel-wise lookup table search that correlates (μ_a, μ_s') with ($R_{d,DC}$, $R_{d,AC}$). The LUT is generated by performing Monte-Carlo simulations of $R_{d,AC}$ at $0.1mm^{-1}$ increments and summing them together to match the range of frequencies sampled by the first two non-zero points of the measured PSD centered at $0.2mm^{-1}$ to $0.4mm^{-1}$, which represent the response from $0.1mm^{-1}$ to $0.5mm^{-1}$. The frequency resolution and the lowest non-DC spatial frequency are affected by the window size. For the window size used in this proof-of-concept study, the PSD frequency resolution is $0.2mm^{-1}$. We assume that each point in the PSD curve represents the integrated response over a band of frequencies. For example, the first non-zero point of the PSD is centered at $0.2mm^{-1}$ and represents the integrated response of the frequencies between $0.1mm^{-1}$ and $0.3mm^{-1}$. We took this into account when constructing the LUT with Monte-Carlo simulations by conducting these simulations at smaller spatial frequency increments than our PSD resolution. For example, to find the response at $0.2mm^{-1}$, we simulated the reflectance at $0.1mm^{-1}$, $0.2mm^{-1}$, and $0.3mm^{-1}$ and used the average of these responses. The same process is performed for the calibration phantom. The data flow is also summarized in Algorithm S1. For comparison, the conventional SFDI processing flow is shown in Algorithm S2.

Algorithm S1. si-SFDI algorithm

procedure SI-SFDI(x, y, r, ss, N, I_i)
  average N patterns (I_i) and smooth to obtain M_{DC}
  subtract M_{DC} from each I_i
  while $(x-d, y-d) > (0,0)$ and $(x+d, y+d) \leq size(I_i)$ **do** ▷ d is window radius
    for $n = 1 : N$ **do**
      extract window ($w_i(x,y)$) with width $= 2d$
      calculate autocorrelation $a_{w_i}(x,y)$
    $a_w(x,y) \leftarrow \frac{1}{N} \cdot \sum_{i=1}^{N} a_{w_i}(x,y)$
    radially average $a_w(x,y)$ to obtain $a_w(r)$
    $S_W(k_r) \leftarrow \mathcal{F}[a_w(r)]$ ▷ $S_W(k_r)$ is power spectral density
    $M_{AC}(x - \frac{ss}{2} : x + \frac{ss}{2}, y - \frac{ss}{2} : y + \frac{ss}{2}) \leftarrow \int_{0.1}^{0.5} \sqrt{S_W(k_r)} dk_r$ ▷ ss is step size
    $x \leftarrow x + ss$
    $y \leftarrow y + ss$
  repeat above steps for reference phantom
  calibrate to obtain $R_{d,DC}$ and $R_{d,AC}$
  fit (μ_a, μ_s') using an LUT
  return μ_a and μ_s'

2. PHANTOM RESULTS

The mismatch in illumination wavelengths (526nm for SFDI and 520nm for si-SFDI) was first corrected using the predicted optical properties of India ink and titanium dioxide. The expected absorption was calculated as $\mu_{a,si-SFDI} = \mu_{a,SFDI,meas} \frac{\epsilon(520nm)}{\epsilon(526nm)} = 1.013\mu_{a,SFDI,meas}$, where ϵ is the extinction coefficient of India ink at the corresponding wavelengths [2]. A Rayleigh scattering relationship ($\mu_s' \propto \lambda^{-4}$) was assumed for μ_s' as the diameter of titanium dioxide nanoparticles was much smaller than the wavelengths used in this study. Thus, the expected scattering coefficient was defined as $\mu'_{s,si-SFDI} = \mu'_{s,SFDI,meas} \frac{(520nm)^{-4}}{(526nm)^{-4}} = 1.047\mu'_{s,SFDI,meas}$. The results of si-SFDI applied on tissue-mimicking phantoms using one and four speckle images are shown in 2-D scatter plots in Figure S1. Compared to one speckle pattern (Figure S1(a)), si-SFDI with four patterns (Figure S1(b)) shows improved accuracy with lower variances. This is expected

Algorithm S2. Conventional SFDI algorithm

procedure SI-SFDI($I_0(x_i, f_x)$, $I_{\frac{2}{3}\pi}(x_i, f_x)$, $I_{\frac{4}{3}\pi}(x_i, f_x)$)

$M(x_i, f_x) \leftarrow$
$\frac{\sqrt{2}}{3}\sqrt{[I_0(x_i, f_x) - I_{\frac{2}{3}\pi}(x_i, f_x)]^2 + [I_{\frac{2}{3}\pi}(x_i, f_x) - I_{\frac{4}{3}\pi}(x_i, f_x)]^2 + [I_{\frac{4}{3}\pi}(x_i, f_x) - I_0(x_i, f_x)]^2}$

▷ x_i is pixel location; f_x is spatial frequency; I_0, $I_{\frac{2}{3}\pi}$, and $I_{\frac{4}{3}\pi}$ are images at three phases

$M_{DC}(x_i) \leftarrow M(x_i, 0)$

$M_{AC}(x_i) \leftarrow M(x_i, 0.2mm^{-1})$

repeat above steps for reference phantom

calibrate to obtain $R_{d,DC}$ and $R_{d,AC}$

fit (μ_a, μ_s') using an LUT

return μ_a and μ_s'

since individual speckle patterns are often noisy and averaging multiple patterns improves the confidence in ACF estimations.

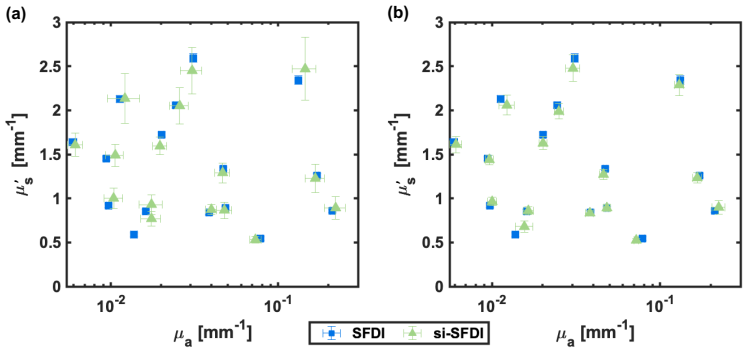

Fig. S1. Scatter plots of phantom optical properties measured by si-SFDI. (a) Results using one speckle pattern. (b) Results using four speckle patterns. SFDI ground truth is shown in both plots. Markers indicate mean values and error bars indicate variance over a central 150×150 pixel region of interest.

Representative PSD plots are also shown in Fig. S2 for five homogeneous phantoms with different optical property pairs. Expected results simulated by Monte-Carlo models are also shown in dashed lines. Our measurements demonstrate strong agreement with simulations, especially for spatial frequencies up to $0.4mm^{-1}$. As expected, the shape of the curves is determined by both μ_a and μ_s'. We observe that the measured PSDs tend to underestimate expected curves. This could be caused by the image filtering described in the si-SFDI processing pipeline, which improves the accuracy of the results but leads to errors at high spatial frequencies.

3. EFFECT OF SURFACE TOPOGRAPHY

To explore the effect of surface topography on the accuracy of si-SFDI, we compare the absolute percentage difference (Fig. S3(a) for μ_a and (b) for μ_s') with surface normal angles (Fig. S3(c)) of the pig esophagus sample. Qualitatively, regions with larger angles are associated with higher error rates. This is expected since the ground truth is profile-corrected SFDI while si-SFDI does not account for surface topography. We additionally plotted the normalized mean absolute error (NMAE) with respect to surface normal angles (Fig. S3(e)). The mean error of si-SFDI is below 20% for relatively flat regions (<10 degrees) and increases with larger tissue angles. Moreover, absorption coefficients appear to be more affected by surface normal angles than reduced scattering, which corresponds to findings in previously published studies [3, 4] and may additionally be due to the window-based approach for calculating M_{AC}. Moreover, theoretically, because of the broader bandwidth of spatial frequencies contained in the illumination pattern, si-SFDI is expected to sample optical properties from a larger axial range than SFDI. Although this was not assessed here, it may warrant further investigation in future studies.

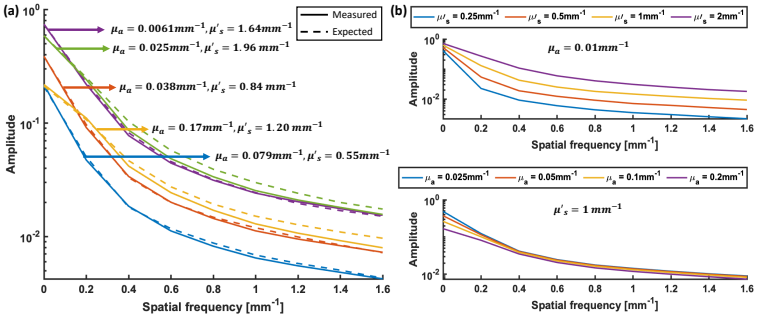

Fig. S2. (a) Representative power spectral density plots for 5 homogeneous phantoms with varying absorption and reduced scattering coefficients. Measured results are plotted in solid lines and simulated data in dashed lines. (b) Top: Simulated PSD plots with fixed μ_a and varying μ_s'; bottom: simulated PSD plots with fixed μ_s' and varying μ_a.

4. EFFECT OF BLOOD FLOW ON SI-SFDI OPTICAL PROPERTY ESTIMATION

To evaluate the effect of blood flow on si-SFDI measurements, we performed an *in vivo* occlusion study where a pressure cuff was applied to an arm for 3 minutes at approximately 200mmHg. Both si-SFDI and SFDI data were acquired before and near the end of occlusion (Fig. S4). This study protocol was approved by Johns Hopkins Institutional Review Board.

To measure the level of blood flow, local speckle contrast (K) is computed within 5×5-pixel sliding windows as the ratio between the standard deviation and mean intensity. As expected, a higher K is observed during occlusion due to reduced blood flow (Fig. S4(g)-(i)). The reduced scattering coefficients at baseline (resting) and occlusion measured by SFDI and si-SFDI ($N = 1$) are shown in Fig. S4(a)-(b) and (d)-(e), respectively. The relative change in μ_s' is shown in (c) and (f). We hypothesize that, while μ_a changes with the level of oxygenation, μ_s' is not affected by occlusion, and thus only μ_s' results are analyzed here. Despite a global increase in speckle contrast during occlusion (approximately 30%), there is not an overall change in μ_s' measured by either SFDI or si-SFDI (less than 1%). Therefore, we conclude that si-SFDI measurements are relatively insensitive to blood flow. This is due to optical properties being a function of the low-spatial frequencies, whereas flowing particles blur the high-spatial frequencies of the illumination. The si-SFDI algorithm described here analyzes the tissue response to spatial frequencies less than $0.5mm^{-1}$. To illustrate this effect, we plot the PSD over a range of spatial frequencies for an ROI with high K contrast changes due to occlusion (Fig. S4(j)). We observe little difference in the PSD between resting and occlusion at the low spatial frequencies used for optical property calculations. The effect of flow becomes more pronounced at spatial frequencies greater than $1mm^{-1}$, with increased attenuation of the PSD at high spatial frequencies due to resting blood flow. This result highlights the potential to image optical properties and flow contrast simultaneously by analyzing different spatial frequency ranges of the computed PSD.

5. DRIFT

We tested the drift of the si-SFDI system by measuring the same phantom every 10 min for 100 min. The standard deviation of the absolute variation in μ_a and μ_s' were 5.54% and 3.15%, which is similar to other SFDI drift results [5] and demonstrates stability of the system over time. An improved laser source with more stable output would further reduce system drift.

6. STEP FUNCTION

To evaluate the resolution of si-SFDI, we record its response to a step function phantom and compare it with conventional SFDI (Fig. S5). The phantom was constructed by cutting two phantoms with different optical properties and press-fitting them together. The resolution is defined to be the distance where the contrast is reduced by 90%. For μ_a, the resolution is 4.1mm for conventional SFDI and 6.3mm for $N = 1$ si-SFDI. For μ_s', the resolution is 2.9mm and 7.3mm for conventional SFDI and $N = 1$ si-SFDI, respectively. μ_s' resolution of si-SFDI is worse than μ_a due to windowing and a stride size larger than 1 pixel.

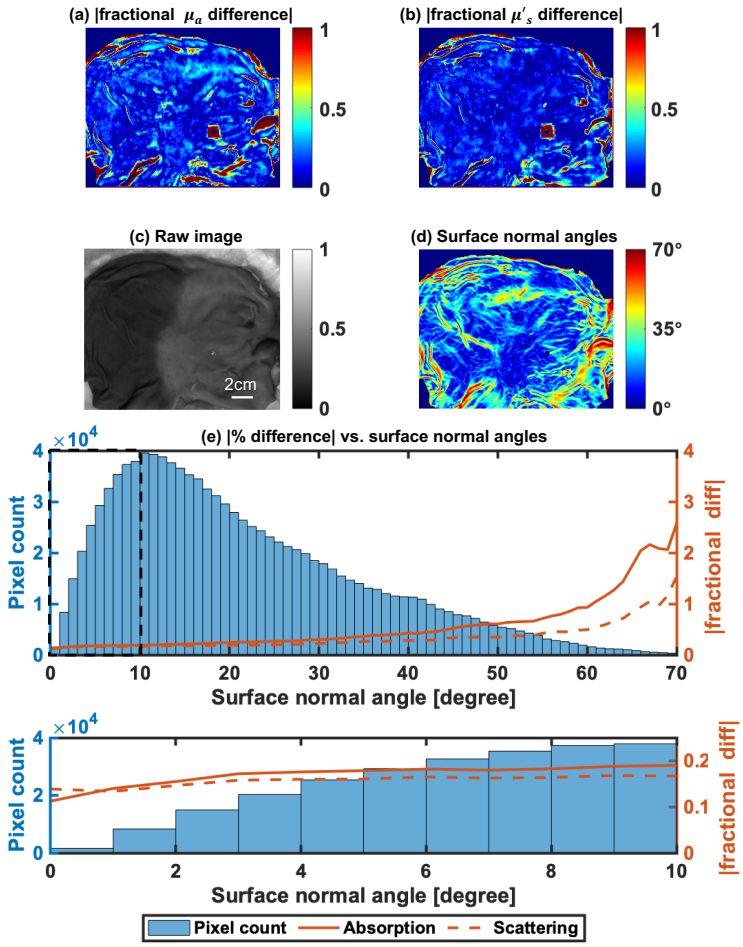

Fig. S3. Absolute percentage difference between si-SFDI and SFDI applied to the full pig esophagus specimen. (a) Absorption error map. (b) Reduced scattering map. (c) Raw image of the sample. (d) Surface normal angles. Background is masked out in (a), (b), and (d). (e) Normalized mean absolute error (NMAE) of si-SFDI as a function of surface normal angles. si-SFDI optical properties are calculated from four input speckle patterns. Top plot in (e) shows the full range, and the region highlighted by the dashed box (between 0 and 10 degrees) is magnified in the bottom plot.

7. FUTURE DIRECTIONS

Potential future directions are discussed here in addition to the main manuscript. For example, a source of discrepancy between SFDI and si-SFDI results is the difference between sampling depth. Theoretically, because of the broader bandwidth of spatial frequencies contained in the illumination pattern, si-SFDI is expected to sample optical properties from a larger axial range than SFDI. Although this was not assessed in this study, it may warrant further investigation in future studies. Moreover, real-time acquisition is imperative for incorporating si-SFDI into future clinical endoscopic applications. For the same illumination power, the exposure time to acquire a single si-SFDI image is similar to conventional SFDI. The total acquisition speed for an optical property estimate depends on the number of speckle patterns used. In the setup used for this study, a 4-image si-SFDI sequence took approximately 2 seconds to acquire. However, for constant power, this speed could be dramatically increased if the object is placed at endoscopic-distances from the camera (typically 2-5cm instead of the 25-30cm tested in our setup). Additional research is needed to study the utility of diffuse and sub-diffuse optical signatures in endoscopic applications. We believe that si-SFDI can be applied to endoscopic measurements of tissue oxygenation by estimating the absorption coefficients at different wavelengths. Scattering coefficients could also

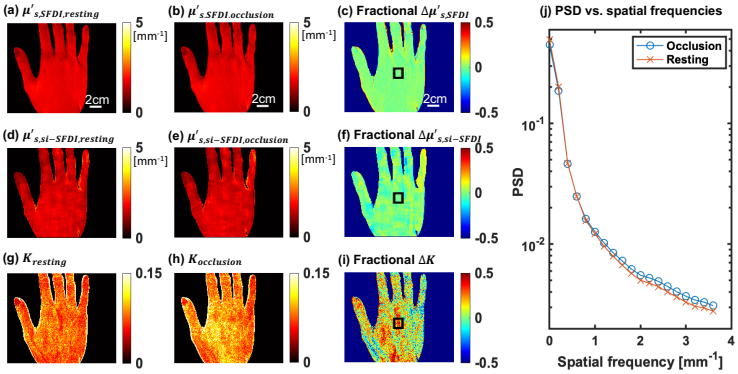

Fig. S4. Occlusion study. (a)-(c): Resting and occlusion μ_s' maps measured by SFDI and the percentage difference; (d)-(f): Resting and occlusion μ_s' maps measured by $N = 1$ si-SFDI and the percentage difference; (g)-(i): Resting and occlusion speckle contrast maps (K) and the relative change. K is computed as the local standard deviation over mean of a 5×5 pixel sliding window; (j): PSD plots for an ROI during resting and occlusion. The ROI is highlighted by the black box in (c), (f), and (i).

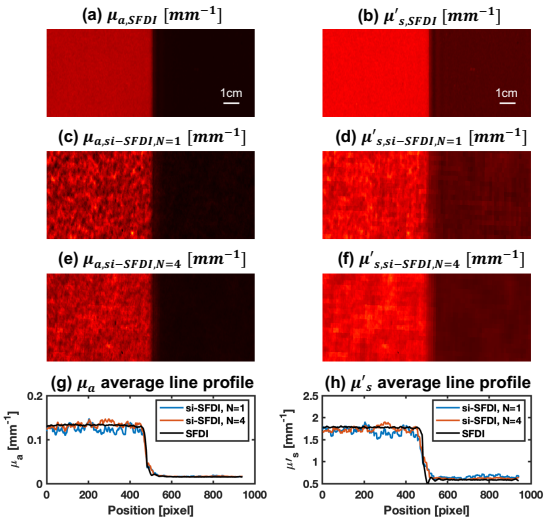

Fig. S5. Response to a step function phantom. Figures in the left column are absorption and figures in the right column are reduced scattering coefficients. From top to bottom: conventional SFDI, si-SFDI with 1 speckle pattern, si-SFDI with 4 speckle patterns, and average line profiles.

be used to distinguish between tissue types, such as benign and malignant tissues [6].

REFERENCES

1. D. J. Cuccia, F. Bevilacqua, A. J. Durkin, F. R. Ayers, and B. J. Tromberg, "Quantitation and mapping of tissue optical properties using modulated imaging," J. Biomed. Opt. **14**, 024012 (2009).
2. P. Di Ninni, F. Martelli, and G. Zaccanti, "The use of india ink in tissue-simulating phantoms," Opt. Express **18**, 26854–26865 (2010).
3. S. Gioux, A. Mazhar, D. J. Cuccia, A. J. Durkin, B. J. Tromberg, and J. V. Frangioni, "Three-Dimensional Surface Profile Intensity Correction for Spatially-Modulated Imaging," J. biomedical optics **14**, 034045 (2009).
4. Y. Zhao, S. Tabassum, S. Piracha, M. S. Nandhu, M. Viapiano, and D. Roblyer, "Angle correction for small animal tumor imaging with spatial frequency domain imaging (sfdi)," Biomed. Opt. Express **7**, 2373–2384 (2016).
5. M. B. Applegate and D. M. Roblyer, "High-speed spatial frequency domain imaging with temporally modulated light," J. Biomed. Opt. **22**, 076019 (2017).
6. A. M. Laughney, V. Krishnaswamy, E. J. Rizzo, M. C. Schwab, R. J. Barth, D. J. Cuccia, B. J. Tromberg, K. D. Paulsen, B. W. Pogue, and W. A. Wells, "Spectral discrimination of breast pathologies in situusing spatial frequency domain imaging," Breast Cancer Res. **15**, R61 (2013).